Lithium Permeation through Thin Lithium–Silicon Films for Battery Applications Investigated by Neutron Reflectometry

Florian Strauß,*[a, b, c] Erwin Hüger,[b] Paul Heitjans,[a, c] Thomas Geue,[d] Jochen Stahn,[d] and Harald Schmidt[b, c, e]

In the ongoing search for new negative electrode materials for lithium-ion batteries, amorphous silicon with a theoretical specific capacity of almost 4000 mA h g^{-1} is still one of the most promising candidates. In order to optimize cycling behavior, prelithiation of silicon is discussed as possible solution. Yet, little is known about kinetics in the Li-Si system, especially with a low lithium content. Using neutron reflectometry as a tool, lithium permeation through amorphous Li_xSi layers was probed during annealing. From the results a lithium permeability (diffusivity × solubility) of $P = (3.3 \pm 0.9) \times 10^{-21}$ m^2 s^{-1} is derived for Li_xSi ($x \approx 0.1$), which is identical to that of pure amorphous silicon.

Introduction

The performance of lithium-ion batteries is to a large extent determined by lithium diffusion in the electrolyte and in the electrode materials. Thus, diffusivities have a major influence on charging and discharging rates, maximum capacity, self-discharge, power density, and cycling stability.[1] Silicon, with a high theoretical capacity of almost 4000 mA h g^{-1}, is under investigation as a possible anode material.[2] The main hindrance for the commercial application of silicon as an electrode material is its extreme volume expansion during lithiation and the connected stress formation and electrode degradation.[3,4] A possible solution is using nanostructured materials in order to minimize stress. To this end, nanowires, nanotubes, and nanoparticles as well as thin films are used.[1,4,5] The improved surface-to-volume ratio in these materials are beneficial for the mitigation of stresses occurring during de-/lithiation. In addition, reducing the lateral dimensions leads to improved electrical contact and a more effective mass transport via diffusion due to the smaller diffusion lengths needed for penetrating the electrode material.[6] Even more promising than crystalline silicon (c-Si) is its amorphous modification. This is mainly due to a reversibility of shape and volume changes during electrode cycling because of a more homogeneous expansion and contraction of amorphous silicon.[7] In this context, an important question is also whether electrode lithiation is a lithium-diffusion- or interface-reaction-controlled process.[8,9] Consequently, a reliable determination of atomic/ionic transport properties is highly desirable.

In order to investigate atomic transport properties, the experimental method described here has already been used to probe pure amorphous silicon (a-Si).[10] However, as amorphous silicon electrodes are lithiated, transport occurs mainly in Li_xSi phases or along Li_xSi interfaces, both exhibiting different structural properties than pure a-Si.[11] While lithium diffusion in various crystalline Li_xSi phases was already probed in the literature by NMR and electrochemical methods,[12–15] no information about amorphous Li_xSi with small values of x is available. Combining the method presented in Ref. [10] with the production of Li_xSi layers with a defined small value of x[16] yields an opportunity to further advance knowledge in this field.

[a] F. Strauß, Prof. Dr. P. Heitjans
Institut für Physikalische Chemie und Elektrochemie
Leibniz Universität Hannover
Callinstr. 3–3a, 30167 Hannover (Germany)
E-mail: strauss.florian@pci.uni-hannover.de

[b] F. Strauß, Dr. E. Hüger, Prof. Dr. H. Schmidt
Institut für Metallurgie
Technische Universität Clausthal
Robert-Koch-Str. 42, 38678 Clausthal-Zellerfeld (Germany)
E-mail: strauss.florian@tu-clausthal.de

[c] F. Strauß, Prof. Dr. P. Heitjans, Prof. Dr. H. Schmidt
ZFM—Zentrum für Festkörperchemie und Neue Materialien
Leibniz Universität Hannover
Callinstr. 3a, 30167 Hannover (Germany)

[d] Dr. T. Geue, Dr. J. Stahn
Laboratory for Neutron Scattering and Imaging
Paul Scherrer Institute
5232 Villigen (Switzerland)

[e] Prof. Dr. H. Schmidt
Clausthaler Zentrum für Materialtechnik
Technische Universität Clausthal
Leibnizstraße 9, 38678 Clausthal-Zellerfeld (Germany)

Supporting Information and the ORCID identification number(s) for the author(s) of this article can be found under http://dx.doi.org/10.1002/ente.201600209.

Part of a Special Issue on "Li-Ion Batteries". To view the complete issue, visit: http://dx.doi.org/10.1002/ente.v4.12

Results and Discussion

As argued before, lithium transport is a decisive factor in battery performance.[8] Transport through a certain layer (e.g., of composition Li_xSi) is governed by the permeability, P, that can be described as the product of the solubility, S, of the transported species in the transport medium and the diffusivity, D. This can be expressed as $P = S \cdot D$.[17] The solubility used here is a unitless quantity, calculated as the number of lithium atoms solute in the Li_xSi phase divided by the total number of atoms. In order to measure lithium permeabilities and thus also diffusivities in Li_xSi, multilayer samples were prepared (see Figure 1), which consisted of $LiNbO_3$ layers

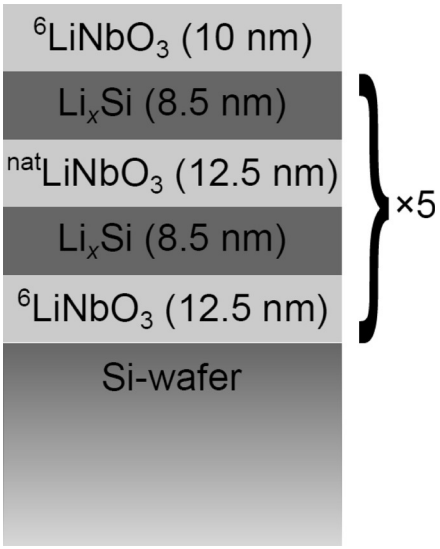

Figure 1. Schematic depiction of the [Li_xSi | $^{nat}LiNbO_3$ | Li_xSi | $^{6}LiNbO_3$]×5 multilayer stack with $x \approx 0.1$, capped by a $^{6}LiNbO_3$ layer. The values given in brackets are the respective thicknesses used for the Parratt32 simulation.

separated by Li_xSi intermediate layers with $x \approx 0.1$. The $LiNbO_3$ layers are alternatingly isotope-enriched ($^{6}LiNbO_3$ or $^{nat}LiNbO_3$, nat: 92.5% ^{7}Li), while Li_xSi always exhibits the natural lithium abundance: ^{nat}Li. The deposited structure is schematically depicted in Figure 1, and the resulting depth distribution of scattering length densities as deduced from neutron reflectivity experiments is shown in Figure 2 while further details can be found in the Experimental Section. In this setup, amorphous $LiNbO_3$ serves solely as lithium tracer reservoir. Amorphous $LiNbO_3$ is a solid electrolyte, exhibiting a high lithium-ion conductivity and diffusivity[18,19] while still retaining a rigid Nb-O skeleton[20] which makes it ideally suited for these experiments. In principle, also other types of materials can be used as tracer reservoirs. The sample design is tailored to neutron reflectometry measurements, which is best explained through Figure 3a. While the isotope contrast from the alternating deposition of $^{6}LiNbO_3$ and $^{nat}LiNbO_3$ gives rise to a distinct Bragg peak around $Q_z \approx 0.019$ Å^{-1} in the reflectivity pattern, the chemical contrast between $LiNbO_3$ and Li_xSi results in an additional Bragg peak at

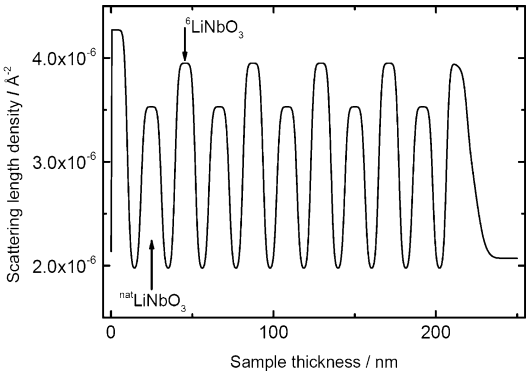

Figure 2. Neutron scattering length density plotted against the sample depth as derived from the Parratt32 simulation of the as-deposited sample. While the maxima are annotated, the minima correspond to the Li_xSi layers.

a higher scattering vector $Q_z \approx 0.033$ Å^{-1}. The continuous line in Figure 3a represents a fit based on calculations using the program Parratt32. With the variation of given input parameters this program uses the Parratt algorithm[21] to simulate the resulting neutron reflectivity pattern. The parameters essential for the simulation are the structure of the sample as given in Figure 1, the thickness of the individual layers as assessed by previously determined sputter rates, and the calculated scattering length densities for the individual layers as shown in Figure 2. The as-deposited sample shown in Figure 3a exhibits the values previously given in Figure 1 and Figure 2.

It is apparent from Figure 3a and b that the overall fit to the experimental data (height and location of the Bragg peaks) is good, but also that some features are not perfectly represented by the simulation output (e.g., the width of the second Bragg peak and the background at higher Q_z). This can mainly be attributed to two simple facts. First, during the neutron experiments the sample is mounted on a ceramic heating plate. Because the absorption of neutrons in silicon is negligible there is a non-negligible contribution of diffusely scattered neutrons due to the heating plate. This adds to the (unknown) background intensity across the whole pattern, evident in the discrepancy between data and fit in the scattering vector range between the two peaks. Second, the fact that the simulation postulates an almost ideal and uniform thickness distribution of layers has to be taken into account. For the simulation of multilayer reflectivities in Parratt32 the repeating element of the sample, in this case the four-layer structure mentioned above, is described by a fixed set of values for thickness, scattering length densities, and roughness of each layer. Of course there is also a statistical variation of thickness and roughness of each individual layer that cannot be fully represented with this type of simulation. However, the alternative route of using a model that considers each layer individually also requires the vetting of many different possible solutions to simulate the given reflectivity pattern due to too many free parameters for the fitting procedure. In the given data set this fact is responsible for the apparent broadening of the chemical contrast peak when

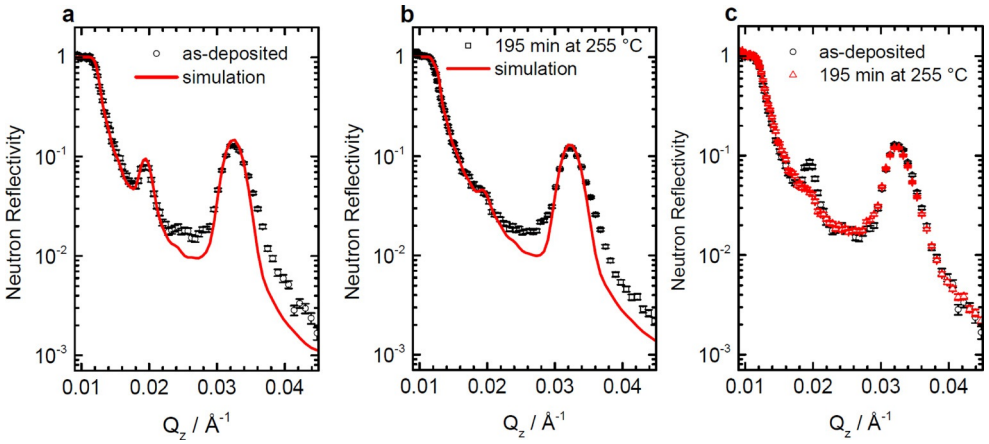

Figure 3. (a) Neutron reflectivity pattern of the sample as shown in Figure 1 in the as-deposited state. The peak around 0.019 $Å^{-1}$ reflects the isotope contrast between the $LiNbO_3$ layers, while the peak around 0.033 $Å^{-1}$ is attributed to the chemical contrast between the individual Li_xSi and $LiNbO_3$ layers. (b) The reflectivity pattern of the sample after annealing at 255 °C for 195 min. In (a) and (b) the circles represent the measured data and the line a least squares fit using Parratt32. (c) Direct comparison of the measured data for the as-deposited (circles) and annealed (triangles) sample.

compared to the simulation curve. The fact that after annealing (see Figure 3c) there is no observable decrease of the chemical peak, independent of the simulation, combined with the fact that the peak due to isotopic contrast decreases significantly means that the fitted data can be used for further analysis in the present case. Background and width of the Bragg peak do not enter the analysis for the determination of permeabilities, only the height of the Bragg peak.

Annealing the sample will lead to diffusion of ^6Li (or ^7Li) isotopes from the $^6LiNbO_3$ (or $^{nat}LiNbO_3$) layers across the interfaces with the Li_xSi layers into and through the Li_xSi layers. It is assumed that no additional lithium (in significant amounts) is dissolved in Li_xSi and only an exchange of isotopes takes place. Because $x \approx 0.1$ and the solubility of lithium in pure a-Si is at least three orders of magnitude lower, as literature data on a-Si:H show,[22] it is safe to say that this only leads to a balancing of the isotope fractions in the lithium reservoirs over time. Figure 3b shows the reflectivity pattern of the same sample annealed for 195 min at 255 °C. The comparison of the data points from Figure 3a and 3b, displayed in Figure 3c, shows that the peak at higher values of Q_z remains essentially unchanged during annealing. A slight decrease during the first annealing step is discussed below. Consequently, the chemical contrast, and thus the chemical composition (and lithium concentration) of the Li_xSi and $LiNbO_3$ layers is not modified significantly. Yet, as soon as $^6Li/^7Li$ isotope interdiffusion sets in, the scattering length density (SLD) of the Li_xSi layer has to be slightly increased (from 2.05×10^{-6} to 2.1×10^{-6} $Å^{-2}$) in the simulation. This effect is attributed to the permeation of the Li_xSi layer by ^6Li atoms and the removal of ^7Li atoms, essentially increasing the ^6Li content in the Li_xSi layer. The bound coherent scattering length of ^6Li is 2.00 fm, while that of ^7Li is −2.22 fm. Thus, even a slight increase in ^6Li content is immediately noticeable. The concentration for each lithium isotope in Li_xSi (after annealing has started) is assessed to 50% on average. This effect leads to the already mentioned decrease of the Bragg peak at $Q_z \approx 0.03$ $Å^{-1}$ (a small, single digit percentage) only present during the first annealing step. No further change to the chemical contrast is observed during additional annealing. It has to be noted that this slight decrease cannot be explained with an increase of the absolute lithium concentration in the Li_xSi layer (increase of x). In that case a peak increase would be expected according to Parratt32 simulations.

At the same time, the peak resulting from the isotopic modulation of the $LiNbO_3$ layers at $Q_z \approx 0.019$ $Å^{-1}$ shows a distinct and continuous decrease during annealing. Simulation of the pattern of the annealed sample is done by adjusting the SLD of both $LiNbO_3$ layers according to a decrease (increase) of the ^6Li content in the respective layer, starting from the values shown in Figure 2. The sum of the scattering length densities of the $LiNbO_3$ layers stays the same but the difference changes. This is concurrent with an advancing equilibration of isotope contents in the differently enriched layers without a change in total Li content and reflects the modification of the relative ^6Li fraction in each $LiNbO_3$ layer. Details can be found in a publication by Hüger et al.[10]

In order to obtain first the permeability and then subsequently the diffusivity the approach introduced by Hüger et al.[10] was applied to the data. In a first step, ^6Li and ^7Li isotope fractions were determined for various annealing times via the simulation described above. The plot of these isotope fractions versus the annealing time is depicted in Figure 4. ^6Li isotope fractions in the $^6LiNbO_3$ layer start out at a value of 92%, concurrent with the isotope enrichment of the layer. After a steady decrease for approximately 3 h of annealing, the ^6Li fraction reaches a plateau at 68%. In parallel, the ^7Li fraction in the $^6LiNbO_3$ starts out at 8%, increases at the same rate, and reaches its plateau at 32% also after 3 h. Except for the slightly different starting values, both lithium isotope fractions in the $^{nat}LiNbO_3$ exactly mirror this behavior. It is further obvious from the plot that the lithium isotopes do not show a complete equilibration at about

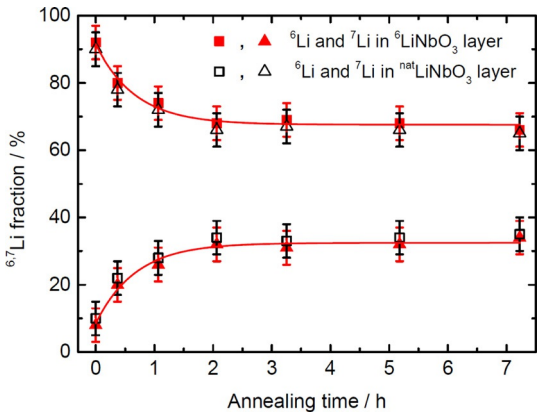

Figure 4. Relative ^{6}Li and ^{7}Li isotope fractions of both $LiNbO_3$ reservoirs, shown as a function of annealing time. Data are obtained from the Parratt32 simulations as explained in the text. Errors were deduced using Parratt32 by varying Li isotope contents of the Li isotope layers until an increase of χ^2 (representing the quality of the fit) of 10% was reached. The scattering length densities were translated into Li isotope fractions resulting in an absolute error of no more than 5%. The fit function is an exponential decay according to Equation (3).

50%. It has to be noted that there is no discernible asymmetry in the lithium isotope fraction development as a function of annealing time comparing the ^{6}Li rich layer and the ^{nat}Li layer. Thus, the assumption that every lithium atom leaving the source layers is compensated by another lithium atom from the neighboring source layer is valid. In the original work by Hüger et al.,[10] this kind of equilibration process was modeled by using the equation

$$\chi_{^6Li} = \frac{\chi^0_{^6Li} + \phi^0_{^6Li}}{2} + \left(\frac{\chi^0_{^6Li} - \phi^0_{^6Li}}{2}\right) \exp[-a(t - t_0)]. \quad (1)$$

Here, $\chi_{^6Li}$ is the isotope fraction of ^{6}Li in the $^{6}LiNbO_3$ layer, $\chi^0_{^6Li}$ is that value at $t=0$, $\phi_{^6Li}$ is the amount of ^{6}Li in the $^{nat}LiNbO_3$ layer at $t=0$, t_0 is a lag time determined by the time it takes lithium to completely diffuse through the (here) Li_xSi layer, and a is given by (already adjusted to the sample configuration used in this study)

$$a = 4\frac{P}{d_{LiSi}d_{LiNbO_3}}\frac{\rho_{LiSi}}{\rho_{LiNbO_3}}\frac{M_{LiNbO_3}}{M_{LiSi}}. \quad (2)$$

Here, P is the permeability of the Li_xSi layer, d_{LiSi} and d_{LiNbO_3} are the respective thicknesses of the Li_xSi layer and of the $LiNbO_3$ source layer, ρ_{LiSi} and ρ_{LiNbO_3} the respective mass densities, and M_{LiNbO_3} and M_{LiSi} the respective molar masses. For the given system, Equation (1) has to be modified in two ways. The initial and final values are no longer expressed as the sum of or difference between isotope contents because that concept is based on a complete equilibration. Applying the fit with values of t_0 ranging between 0 and 15 min did not change the parameter a beyond the error limits. Thus, the lag time t_0 is omitted in the equation used to fit the data. Consequently, the fit function applied to the data was

$$\chi_{^6Li} = \chi^{final}_{^6Li} + B\exp[-at] \quad (3)$$

In this case, $\chi^{final}_{^6Li}$ is the value at which the isotope equilibration stops and B is the amplitude of the function.

Applying those fit functions to the data shown in Figure 4, in both cases a parameter $a=(1.5\pm0.2)\,h^{-1}$ [i.e., $(4.2\pm0.6)\times10^{-4}\,s^{-1}$] and, using Equation (2), a permeability of $P=(3.3\pm0.9)\times10^{-21}\,m^2\,s^{-1}$ is obtained. The lack of a complete equilibration to values of about 50% for both fractions might be due to a time-dependent diffusivity process or a two stage equilibration process, but further measurements are needed for clarification.

In the experimental study on a-Si by Hüger et al.,[10] a permeability of $(1.3\pm0.2)\times10^{-21}\,m^2\,s^{-1}$ was derived at 240 °C using the analogous setup.[23] A direct comparison to the value of $(3.3\pm0.9)\times10^{-21}\,m^2\,s^{-1}$ found in this study shows that the addition of about 10 at% of lithium to silicon in the Li_xSi layer does not significantly change the permeability of the system. This result is astonishing because due to the higher lithium solubility that can be expected in Li_xSi ($S=0.09$) compared to amorphous silicon containing some percent of hydrogen ($S=(2\pm1)\times10^{-4}$ at 240 °C[22]), an about three orders of magnitude lower diffusivity can be expected for Li_xSi using $D=P/S$. This is an obviously extreme discrepancy to previous findings in literature as shown in Figure 5.

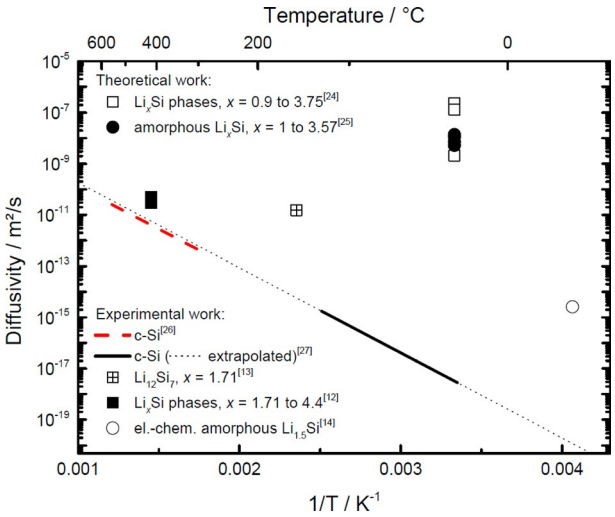

Figure 5. Literature data on Li diffusivities in crystalline silicon (c-Si) and various crystalline and amorphous Li_xSi phases as a function of inverse temperature. Data points for crystalline phases are represented by squares, amorphous phases by circles. The data clearly illustrates the fact that the addition of Li into Si leads to enhanced Li diffusivities. Especially recent theoretical calculations[24,25] emphasize the increase of ***D*** with the increase of ***x*** in Li_xSi.

Larue[26] and Pell[27] have reported on lithium diffusion in c-Si at temperatures slightly above and below the 255 °C used in the experiments presented here. However, comparing the extrapolated data gives a good agreement of their findings to each other. The addition of lithium to the crystalline matrix was directly probed by Dunst et al.[14] who, using NMR at −30 °C, found for electrochemically amorphousized $Li_{1.5}Si$ a diffusivity that surpasses the extrapolated value from Larue[26] and Pell[27] by about five orders of magnitude. Kuhn

et al.[13] reported a diffusivity in $Li_{12}Si_7$ also obtained by NMR at 150 °C that is still larger than the extrapolated values by three orders of magnitude. Even the findings by Wen et al. in various crystalline LiSi phases[12] at 400 °C still surpass the extrapolated c-Si data by about one order of magnitude. So at least for c-Si it is indicated that the addition of a significant amount of lithium enhances the lithium diffusivity. Additionally, ab initio molecular dynamics calculations done for various compositions of Li_xSi alloys showed a strong dependence of the lithium ion diffusivity on the lithium content of the alloy.[25] Diffusivities increased by two orders of magnitude at room temperature by increasing x from 1 to 3.75. Similar calculations by Chiang et al.[24] show a comparable behavior for amorphous Li_xSi with diffusivities also increasing by one order of magnitude with an increase in x from 1 to 3.57, showing a pronounced dependence on lithium content.

These literature data indicate that the addition of Li to silicon (Si→Li_xSi) or the increase of x in Li_xSi leads to enhanced lithium diffusivities in the material. While literature data are diffusivities, the data presented here are permeabilities because the necessary solubilities to calculate the diffusivities are not known.

Concerning the literature work, the most likely explanation for our results is that the sample with a low lithium content of $x \approx 0.1$ in Li_xSi does not exhibit a percolation path for lithium diffusion along a lithium–silicon network if the lithium atoms are statistically distributed in the silicon matrix. Consequently, diffusion of lithium will take place along a pure a-Si network. This will explain the similar permeability. The diffusing lithium only penetrates along a-Si domains with the same solubility and diffusivity as in pure a-Si. Consequently, the same permeability as reported by Hüger et al.[10,23] is measured within error limits (neglecting the slight temperature difference of 15 °C).

Conclusions

Lithium permeation through thin Li_xSi layers sandwiched between isotopically modulated $LiNbO_3$ layers, serving as tracer reservoirs in a multilayer structure, was observed using neutron reflectometry with a rapid thermal annealing setup. Two distinct Bragg peaks are observable in the reflectivity pattern. One is attributable to the chemical contrast between the Li_xSi layers and the $LiNbO_3$ layer, the other to the isotope contrast between the $^6LiNbO_3$ and $^{nat}LiNbO_3$ layers. Annealing at 255 °C in argon atmosphere leads to lithium isotope interdiffusion through the Li_xSi layer from one inert $LiNbO_3$ layer to the other and, consequently, to a de-/increase in $^{6/7}Li$ fractions in the $LiNbO_3$ layers. This in turn leads to a decrease of the corresponding peak, which can be used to assess lithium permeabilities of the Li_xSi layer. During the whole process, the chemical contrast remains unchanged, a fact that is reflected by a constancy of the corresponding reflectivity peak. The permeability of Li through Li_xSi with $x \approx 0.1$ at 255 °C is found to be $P = (3.3 \pm 0.9) \times 10^{-21}\,m^2\,s^{-1}$ which is the same as that reported for pure a-Si. Thus, diffusion is expected to occur in pure a-Si domains and not along lithium–silicon-rich percolation paths.

Experimental Section

Samples

The sample material used in this investigation was a multilayer arrangement consisting of five sets of [Li_xSi (8.5 nm) | $^{nat}LiNbO_3$ (12.5 nm) | Li_xSi (8.5 nm) | $^6LiNbO_3$ (12.5 nm)] units subsequently deposited by ion-beam sputtering onto an appropriate silicon wafer substrate and capped by an additional $^6LiNbO_3$ layer. The Li_xSi layers were prepared as described in a previous publication by reactive co-sputtering of lithium foil and a silicon wafer.[16] The target design was modified in comparison to the original experiment[16] so that a reduction of Li content in Li_xSi to about $x \approx 0.1$ was achieved, which was verified by secondary ion mass spectrometry measurements in combination with X-ray photoelectron spectroscopy. The corresponding data can be found in the Supporting Information. The amorphous $LiNbO_3$ layers were sputtered from two sintered polycrystalline targets exhibiting different lithium isotope enrichment but the layers still maintained a composition and isotope concentration close to the $LiNbO_3$ target material.[19,28] Consequently, layers termed $^{nat}LiNbO_3$ have a composition of $^7Li_{0.925}{}^6Li_{0.075}NbO_3$ while layers termed $^6LiNbO_3$ are composed of $^7Li_{0.08}{}^6Li_{0.92}NbO_3$.

Preparation technique

Sputtering was done by using a commercial ion-beam sputter coater IBC 681 (Gatan, USA) with argon as sputter gas. The acceleration voltage was set to 5 kV with a beam current of 200 μA. Base pressure was below 5×10^{-7} mbar and did not surpass 1×10^{-4} mbar during deposition. The sputter coater was set up in an argon filled glovebox so as to minimize atmospheric contamination. All three targets were mounted in the coater at the same time. Consequently, deposition could be done without exposing the samples to anything but the conditions inside the sputter coater.

Annealing

Annealing was done in an AO500 rapid thermal annealing setup (MBE components) which was modified to allow neutron reflectometry measurements without removing the sample from the oven. Thus, orientation and position of the sample were kept unchanged at all times during those measurements. In order to reduce diffuse scattering by the ceramic heating plate, an additional silicon wafer with a thickness of 1 mm was put below the sample. Notably, diffuse scattering was not avoided but only reduced. As a consequence, an additional calibration of this setup was performed to gauge the correct temperatures.

Neutron reflectometry

Neutron reflectometry measurements were performed at SINQ, Villigen, Switzerland, on the time-of-flight reflectometer AMOR in the recently implemented Selene setup.[29] In comparison to the conventional setup of the instrument, where either angle or wavelength is kept fixed, incident angle and wavelength of the neutron beam can be varied at the same time. To achieve this, the wavelength is determined by time-of-flight, and the scattering

angle via a position sensitive detector. Additionally, the Selene waveguide provides a focused neutron beam with a wider divergence, that is, a wider range of incident angles. Consequently, measuring time is reduced by more than one order of magnitude for small values of Q_z.

Acknowledgements

This work is based on experiments performed on the neutron reflectometer AMOR at the Swiss spallation neutron source SINQ, Paul Scherrer Institute, Villigen, Switzerland. Financial support by the Niedersächsisches Ministerium für Wissenschaft und Kultur (MWK) within Graduiertenkolleg Energiespeicher und Elektromobilität Niedersachsen (GEENI, contract ZN2783) is gratefully acknowledged. E.H. gratefully acknowledges financial support from the Deutsche Forschungsgemeinschaft (DFG) under the contract HU 2170/2-1.

Keywords: diffusivity · energy materials · neutron reflectometry · permeability · thin films

[1] *High Energy Density Lithium Batteries. Materials, Engineering, Applications* (Ed.: K. E. Aifantis), Wiley-VCH, Weinheim, **2010**.
[2] M. T. McDowell, S. W. Lee, W. D. Nix, Y. Cui, *Adv. Mater.* **2013**, *25*, 4966–4985.
[3] a) B. A. Boukamp, *J. Electrochem. Soc.* **1981**, *128*, 725; b) B. Jerliu, E. Hüger, L. Dörrer, B.-K. Seidlhofer, R. Steitz, V. Oberst, U. Geckle, M. Bruns, H. Schmidt, *J. Phys. Chem. C* **2014**, *118*, 9395–9399.
[4] J. R. Szczech, S. Jin, *Energy Environ. Sci.* **2011**, *4*, 56–72.
[5] T. Song, J. Xia, J.-H. Lee, D. H. Lee, M.-S. Kwon, J.-M. Choi, J. Wu, S. K. Doo, H. Chang, W. I. Park, D. S. Zang, H. Kim, Y. Huang, K.-C. Hwang, J. A. Rogers, U. Paik, *Nano Lett.* **2010**, *10*, 1710–1716.
[6] T. T. Truong, Y. Qin, Y. Ren, Z. Chen, M. K. Chan, J. P. Greeley, K. Amine, Y. Sun, *Adv. Mater.* **2011**, *23*, 4947–4952.
[7] L. Y. Beaulieu, T. D. Hatchard, A. Bonakdarpour, M. D. Fleischauer, J. R. Dahn, *J. Electrochem. Soc.* **2003**, *150*, A1457.
[8] M. Park, X. Zhang, M. Chung, G. B. Less, A. M. Sastry, *J. Power Sources* **2010**, *195*, 7904–7929.
[9] M. T. McDowell, S. W. Lee, J. T. Harris, B. A. Korgel, C. Wang, W. D. Nix, Y. Cui, *Nano Lett.* **2013**, *13*, 758–764.
[10] E. Hüger, L. Dörrer, J. Rahn, T. Panzner, J. Stahn, G. Lilienkamp, H. Schmidt, *Nano Lett.* **2013**, *13*, 1237–1244.
[11] M. N. Obrovac, L. Christensen, *Electrochem. Solid-State Lett.* **2004**, *7*, A93.
[12] C. J. Wen, R. A. Huggins, *J. Solid State Chem.* **1981**, *37*, 271–278.
[13] A. Kuhn, P. Sreeraj, R. Pöttgen, H.-D. Wiemhöfer, M. Wilkening, P. Heitjans, *J. Am. Chem. Soc.* **2011**, *133*, 11018–11021.
[14] A. Dunst, M. Sternad, V. Epp, M. Wilkening, *J. Phys. Chem. C* **2015**, *119*, 12183–12192.
[15] A. Kuhn, S. Dupke, M. Kunze, S. Puravankara, T. Langer, R. Pöttgen, M. Winter, H.-D. Wiemhöfer, H. Eckert, P. Heitjans, *J. Phys. Chem. C* **2014**, *118*, 28350–28360.
[16] F. Strauß, E. Hüger, P. Heitjans, V. Trouillet, M. Bruns, H. Schmidt, *RSC Adv.* **2015**, *5*, 7192–7195.
[17] J. Crank, *The Mathematics of Diffusion*, Oxford University Press, **1979**.
[18] P. Heitjans, M. Masoud, A. Feldhoff, M. Wilkening, *Faraday Discuss.* **2007**, *134*, 67–82.
[19] J. Rahn, E. Hüger, L. Dörrer, B. Ruprecht, P. Heitjans, H. Schmidt, *Z. Phys. Chem.* **2012**, *226*, 439–448.
[20] T. Volk, M. Wöhlecke, *Lithium Niobate. Defects, Photorefraction and Ferroelectric Switching*, Springer, Berlin, **2008**.
[21] L. G. Parratt, *Phys. Rev.* **1954**, *95*, 359.
[22] U. Zastrow, W. Beyer, J. Herion, *Fresenius J. Anal. Chem.* **1993**, *346*, 92–95.
[23] E. Hüger, J. Stahn, H. Schmidt, *J. Electrochem. Soc.* **2015**, *162*, A7104–A7109.
[24] H.-H. Chiang, J.-M. Lu, C.-L. Kuo, *J. Chem. Phys.* **2016**, *144*, 034502.
[25] Z. Wang, Q. Su, H. Deng, Y. Fu, *ChemElectroChem* **2015**, *2*, 1292–1297.
[26] J. C. Larue, *Phys. Stat. Solidi A* **1971**, *6*, 143–151.
[27] E. M. Pell, *Phys. Rev.* **1960**, *119*, 1222.
[28] J. Rahn, E. Hüger, L. Dörrer, B. Ruprecht, P. Heitjans, H. Schmidt, *Phys. Chem. Chem. Phys.* **2012**, *14*, 2427.
[29] a) J. Stahn, U. Filges, T. Panzner, *Eur. Phys. J. Appl. Phys.* **2012**, *58*, 11001; b) J. Stahn, T. Panzner, U. Filges, C. Marcelot, P. Böni, *Nucl. Instrum. Methods Phys. Res. Sect. A* **2011**, *634*, S12–S16.

Received: March 23, 2016
Revised: May 24, 2016
Published online on August 16, 2016

